UC Berkeley
UC Berkeley Previously Published Works

Title

Atlantic Meridional Overturning Circulation (AMOC) in CMIP5 Models: RCP and Historical Simulations

Permalink

Journal

ISSN

Authors

Cheng, Wei
Chiang, John CH
Zhang, Dongxiao

Publication Date

2013-09-15

DOI

Peer reviewed

Atlantic Meridional Overturning Circulation (AMOC) in CMIP5 Models: RCP and Historical Simulations

WEI CHENG

Joint Institute for the Study of the Atmosphere and Ocean, University of Washington, and Pacific Marine Environmental Laboratory, Seattle, Washington

JOHN C. H. CHIANG

Department of Geography, and Berkeley Atmospheric Sciences Center, University of California, Berkeley, Berkeley, California

DONGXIAO ZHANG

Joint Institute for the Study of the Atmosphere and Ocean, University of Washington, and Pacific Marine Environmental Laboratory, Seattle, Washington

(Manuscript received 26 July 2012, in final form 29 December 2012)

ABSTRACT

The Atlantic meridional overturning circulation (AMOC) simulated by 10 models from phase 5 of the Coupled Model Intercomparison Project (CMIP5) for the historical (1850–2005) and future climate is examined. The historical simulations of the AMOC mean state are more closely matched to observations than those of phase 3 of the Coupled Model Intercomparison Project (CMIP3). Similarly to CMIP3, all models predict a weakening of the AMOC in the twenty-first century, though the degree of weakening varies considerably among the models. Under the representative concentration pathway 4.5 (RCP4.5) scenario, the weakening by year 2100 is 5%–40% of the individual model's historical mean state; under RCP8.5, the weakening increases to 15%–60% over the same period. RCP4.5 leads to the stabilization of the AMOC in the second half of the twenty-first century and a slower (then weakening rate) but steady recovery thereafter, while RCP8.5 gives rise to a continuous weakening of the AMOC throughout the twenty-first century. In the CMIP5 historical simulations, all but one model exhibit a weak downward trend [ranging from -0.1 to -1.8 Sverdrup (Sv) century^{-1}; 1 Sv $\equiv 10^6 \, \mathrm{m^3 \, s^{-1}}$] over the twentieth century. Additionally, the multimodel ensemble–mean AMOC exhibits multidecadal variability with a ~60-yr periodicity and a peak-to-peak amplitude of ~1 Sv; all individual models project consistently onto this multidecadal mode. This multidecadal variability is significantly correlated with similar variations in the net surface shortwave radiative flux in the North Atlantic and with surface freshwater flux variations in the subpolar latitudes. Potential drivers for the twentieth-century multimodel AMOC variability, including external climate forcing and the North Atlantic Oscillation (NAO), and the implication of these results on the North Atlantic SST variability are discussed.

1. Introduction

The Atlantic meridional overturning circulation (AMOC) plays an important role in regulating the earth's climate. Changes in the AMOC can impact, for example, the North Atlantic storm tracks (Woollings et al. 2012), North American and European summer climate (Sutton and Hodson 2005), the intertropical convergence zone (Vellinga and Wood 2002; Cheng et al. 2007; Chiang et al. 2008), African and Indian monsoon rainfall (Zhang and Delworth 2006), sea level rise (Levermann et al. 2005; Hu et al. 2011), and ocean CO_2 sequestration (Sabine et al. 2004). The strength of the AMOC in the late twentieth century has been inferred using chlorofluorocarbon (CFC) inventories (Smethie and Fine 2001), global inverse modeling (Ganachaud 2003; Lumpkin and Speer 2007), and ocean hydrographic surveys (Talley et al. 2003). The ongoing Rapid Climate Change–Meridional Overturning Circulation and Heatflux Array (RAPID–MOCHA) at 26.5°N (Rayner et al. 2011)

provides a continuous monitoring of the AMOC from 2004 to the present. These data already offer new insights into the spatial and temporal structures of the AMOC and associated meridional heat transport (Cunningham et al. 2007; Bryden et al. 2009; Kanzow et al. 2010; Johns et al. 2011); they also give a valuable reference for validating climate model output.

Phase 3 of the Coupled Model Intercomparison Project (CMIP3) revealed a wide spread in the simulated twenty-first-century AMOC strength (Gregory et al. 2005; Meehl et al. 2007; Schmittner et al. 2005; Schneider et al. 2007). The mean twentieth-century AMOC strength ranges from less than 10 to 25 Sverdrup (Sv; $1\,Sv \equiv 10^6\,m^3\,s^{-1}$). These results highlight the uncertainty associated with assessing and predicting the AMOC state. Recently, the successor, phase 5 of the Coupled Model Intercomparison Project (CMIP5), has become available, providing multimodel simulations of historical and future scenarios all under a common forcing framework (Taylor et al. 2012). The climate models participating in CMIP5 are more comprehensive; many include interactive biogeochemical components and prognostic rather than imposed aerosol concentrations. CMIP5 also made available a large number of ensemble runs necessary for extracting externally forced AMOC variability, if any, given the strong internal variability of the AMOC (Delworth et al. 1993; Cheng et al. 2004, 2007; Kwon and Frankignoul 2012; Danabasoglu et al. 2012; Delworth et al. 2012). In this study, we examine the AMOC mean state and temporal variability in CMIP5 simulations, with a focus on understanding the multimodel ensemble–mean behavior.

2. Data and results

We used the meridional mass transport streamfunction output from 10 models in CMIP5 that were available for analysis by 30 April 2012. Table A1 in the appendix gives a list of the model names and expansions, their ensemble run numbers, and run lengths. We used output from both the ''historical'' (year 1850–2005) and representative concentration pathway (RCP) simulations of these models, using only the RCP4.5 and RCP8.5 scenarios because they had better model coverage.

a. RCP runs

The AMOC index was defined as the annual-mean maximum volume transport streamfunction at 30°N [units in Sverdrups (Sv)]. Of the 10 models, 9 show a mean value of AMOC over the twentieth century that is within the uncertainty range of the AMOC amplitude measured by the RAPID–MOCHA array (Fig. 1). This may be an improvement relative to the CMIP3 simulations (Solomon et al. 2007, their Fig. 10.15); though, it remains to be seen

if this holds true once all CMIP5 output becomes available. Under RCP4.5 forcing, half of the models predict a weakening of the AMOC in the first half of the twenty-first century (Fig. 1a); a majority of the models also show a stabilization of AMOC in the second half of twenty-first century and subsequent rebound (Fig. 1a). In terms of percentage decrease relative to each model's historical average, the magnitude ranges from 5% to 40% by year 2100 (Fig. 1c) under RCP4.5 scenario. Under RCP8.5 forcing, all but one model's AMOC decreases to below the low end of the modern-day observations by 2100 (Fig. 1b), where the percentage decrease ranges from 15% to 60% (Fig. 1d). One model run extends to year 2300 under RCP8.5 forcing; in this model, the AMOC shows stabilization around year 2200 and a slight increase thereafter. The mean percentage decrease of the AMOC in the twenty-first century from CMIP5 is in good agreement with CMIP3 results (Schmittner et al. 2005; Schneider et al. 2007).

b. Historical runs

Anomalies of the AMOC index (throughout this paper, anomaly is defined as deviations from the mean averaged over the entire historical period of 1850–2005) from all models are shown in Fig. 1e. Interannual variability of the AMOC in most models is within a few Sverdrups, although the Geophysical Fluid Dynamics Laboratory (GFDL-ESM2M and GFDL CM3) and Max Planck Institute (MPI-ESM-LR and MPI-ESM-P) models show a stronger multidecadal variation (not shown). The multimodel ensemble–mean (taken over 41 ensemble members from 10 models) AMOC anomaly shows a multidecadal variation with a period of ~60 yr (Figs. 2a,b) and a peak-to-peak range slightly less than 1 Sv. To examine whether this multidecadal variation is common across all models, we performed a combined EOF analysis where all models' AMOC index anomaly is combined into one matrix for eigenvalue decomposition. The first and second mode explains 44.2% and 27.2% of the total variance, respectively: well separated from the higher modes (not shown).

The principal component of mode 1 (PC1) represents a downward trend (Fig. 3a), and PC of mode 2 (PC2) represents a multidecadal variation (solid line in Fig. 3c) closely resembling the multimodel ensemble–mean AMOC (dashed line in Fig. 3c). All models project onto these leading EOF modes with the same sign, except model 8 (GFDL CM3), which shows a strengthening trend over the twentieth century (as indicated by the negative eigenvalue corresponding to model 8 in Fig. 3b). The spatial AMOC anomaly associated with mode 2 is a single cell extending from 75°N to the South Atlantic, with the vertical movement situated between 65° and 45°N
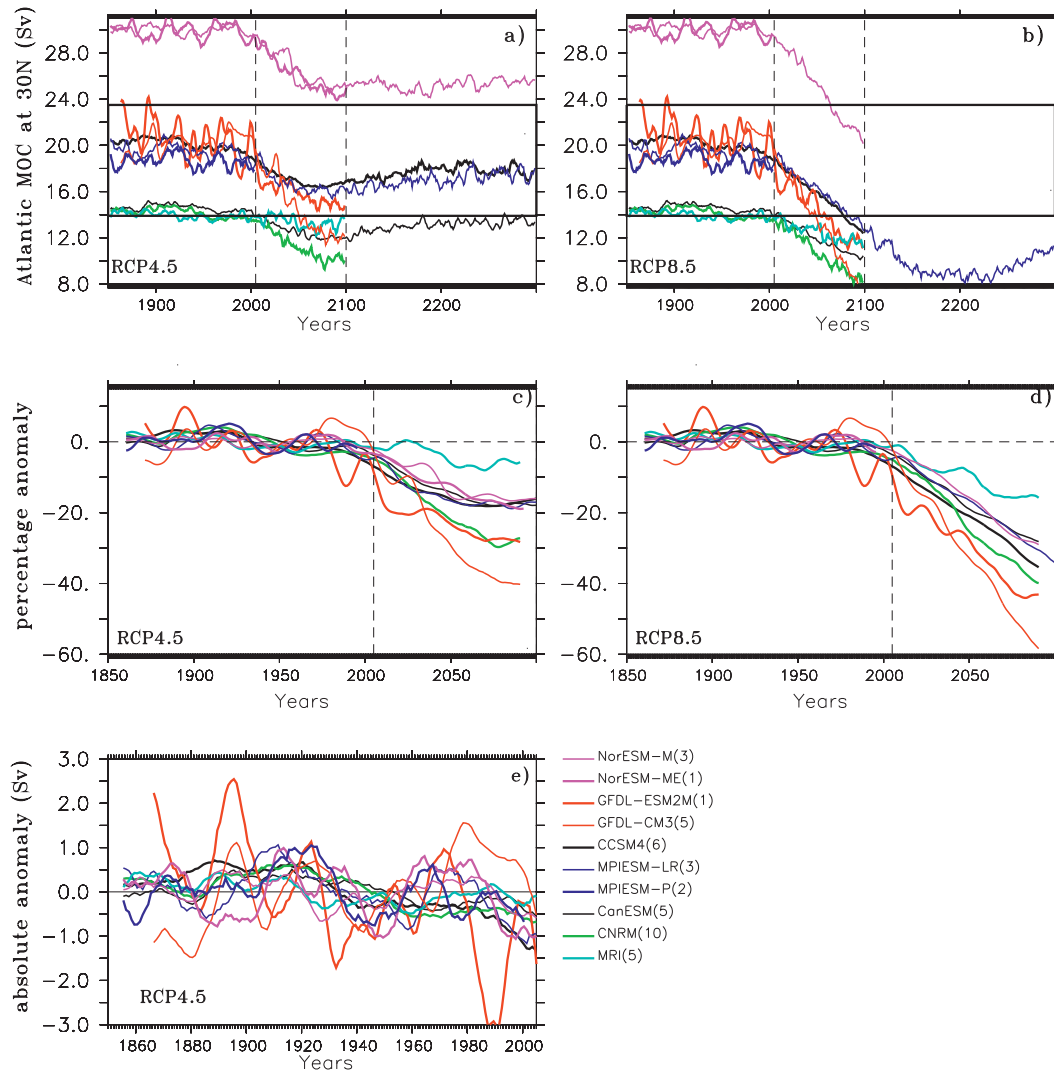
FIG. 1. The AMOC index is defined as the time series of annual-mean maximum volume transport streamfunction at 30°N (Sv). Model names are listed along with the line legends; the numbers in the parentheses indicate ensemble runs available for each model's historical simulations. All time series were averaged over each model's ensemble runs. Absolute values of the AMOC index from historical plus (a) RCP4.5 and (b) RCP8.5 simulations. The annual time series data are filtered by a 5-yr running mean. Horizontal lines in (a) and (b) mark the observed AMOC by the RAPID data and its uncertainty range (18.7 ± 4.8 Sv). (c),(d) Percentage changes in the AMOC index relative to each model's historical mean. The annual time series is filtered by applying an 11-yr running mean twice; years after 2100 were not included because of limited model output. (e) The absolute AMOC anomalies (Sv), relative to each model's historical mean, in years 1850–2005; the original annual time series was filtered by an 11-yr running mean.

(Fig. 4). The anomalous surface flow is concentrated in the top 1000 m, and the anomalous deep flow is between 2000 and 4500 m. There is also a weak anomaly associated with the Antarctic Bottom Water reaching the equator. It is worth noticing that using observed upper-ocean density gradient changes, Wang et al. (2010) inferred a strengthening of the AMOC from 1955 to 2006.

3. Surface flux changes associated with the twentieth-century ensemble-mean AMOC multidecadal variability

What drives the multidecadal variations of the multimodel ensemble–mean AMOC? Broadly speaking, the AMOC magnitude is controlled by surface buoyancy flux, ocean internal mixing, and surface momentum
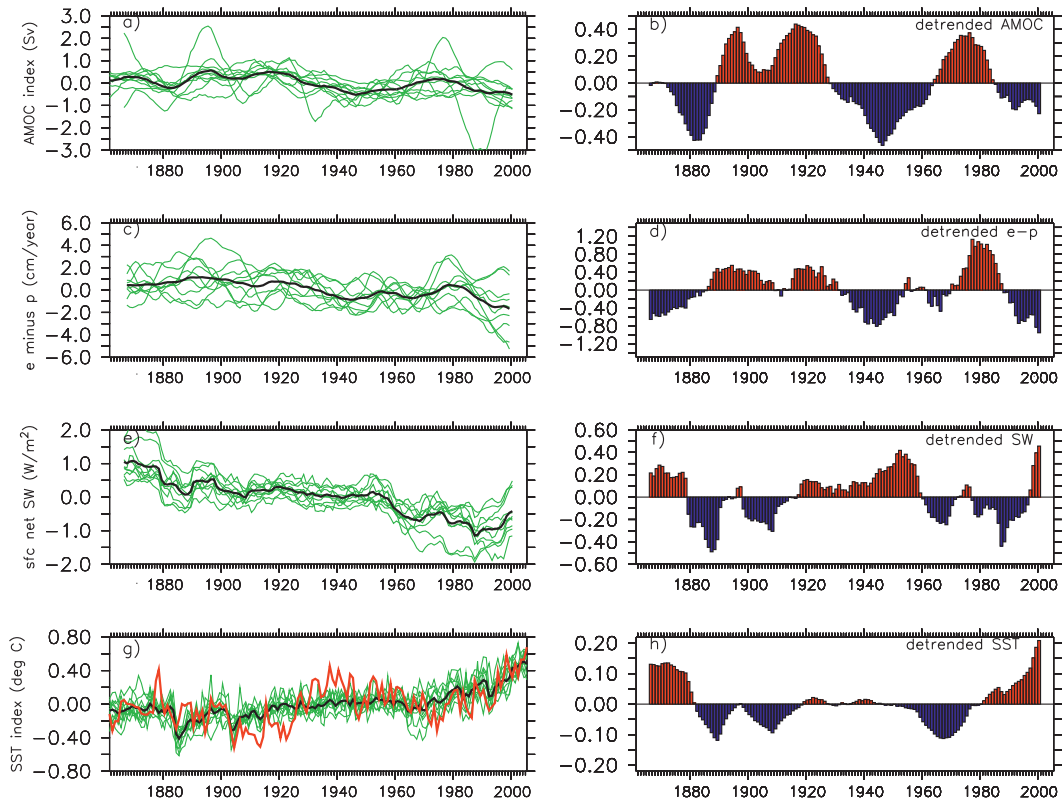
FIG. 2. Climate indices in the North Atlantic. (a) The AMOC index anomalies from each model's ensemble mean (green lines) and the multimodel average (black line). (b) Black line as in (a), but with the linear trend from 1850 to 2005 removed. (c) Annual-mean surface freshwater flux anomalies averaged over the subpolar North Atlantic (40°–60°N, 75°–7.5°W) from each model (green lines) and the multimodel average (black line). (d) Black line as in (c), but with the linear trend from 1850 to 2005 removed. (e) Annual net surface shortwave radiation flux anomalies averaged over the North Atlantic (0°–60°N, 75°–7.5°W), positive indicates downward. Green lines are from each model's ensemble mean and black line is the multimodel average. (f) Black line as in (e), but with the linear trend from 1850 to 2005 removed. (g) Annual SST anomalies averaged over the North Atlantic (0°–60°N, 75°–7.5°W). Green lines are from each model's ensemble average and black line is the multimodel mean; red line is from the extended reconstructed SST (ERSST) dataset. (h) Black line as in (g), but with the linear trend from 1850 to 2005 removed. Green and red lines in the left panels were filtered with an 11-yr running mean.

fluxes. On multidecadal time scales, surface buoyancy forcing likely plays a significant role; in this section, we examine the behavior of surface freshwater and shortwave fluxes in the North Atlantic.

a. Surface freshwater flux

We first examine surface freshwater flux (evaporation − precipitation − runoff, hereafter referred to as $E − P$) in the subpolar North Atlantic (40°–60°N, 75°–7.5°W) (Fig. 2c). The multimodel ensemble–mean $E − P$ anomaly (Fig. 2d) is significantly correlated with the multimodel-mean AMOC anomaly (Fig. 2b), but the maximum correlation occurs when the AMOC variation leads the $E − P$ variation by roughly 2 yr (Fig. 5, dashed-dotted line). This seems counterintuitive at first if the AMOC variability is driven by surface $E − P$ variations. However, because of the feedbacks between the AMOC and

subpolar latitude $E − P$, the phase relationship between them is different from what one might expect based on one-way forcing alone. The strengthening of the AMOC is associated with a northward shift of the Gulf Stream and stronger northward heat transport (e.g., Joyce and Zhang 2010); as a result, positive SST anomalies develop in the subpolar latitudes (Fig. 6c), causing even more evaporation in the region. The positive feedbacks between the AMOC and subpolar $E − P$ variability are reflected in the symmetrical shape of their cross correlation around zero lag (Fig. 5, dashed-dotted line), where the correlation coefficients have the same sign at both positive and negative lags.

b. Surface shortwave flux

We next examine surface shortwave radiation flux and sea surface temperature anomalies in the North Atlantic
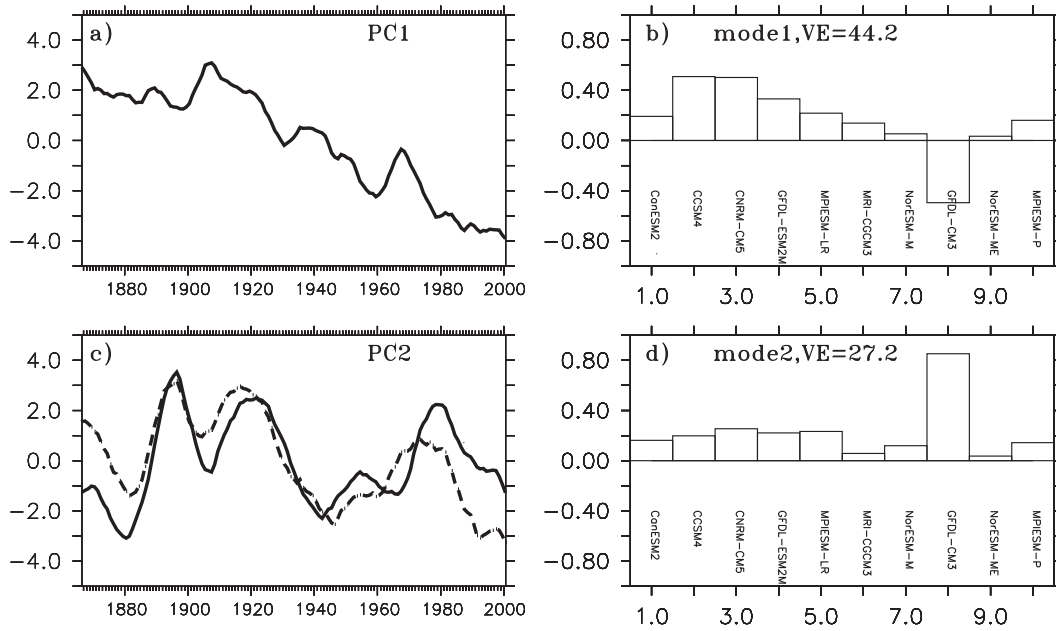
FIG. 3. Eigenvalue decomposition of multimodel AMOC indices. We multiplied each model's ensemble-mean AMOC index anomalies by $\sqrt{N}$, where N is the number of ensemble runs for each model. The resulting anomalies were combined into a single matrix and eigenvalue decomposition was performed on this matrix. The combined EOF modes extract contributions from each model on common principal components across all models. (a),(c) First two principal components and (b),(d) eigenvalues are shown. The x axis in the right panels corresponds to the 10 models used in this study. Variance explained by each mode is marked on the right panels. The dashed line in (c) is the original multimodel ensemble–mean AMOC index anomaly (scaled by a factor of 6 for displaying purposes).

in the multimodel runs. Because surface shortwave flux is not directly a function of SST, it represents an external forcing factor on the ocean. The shortwave radiation flux and SST time series (Figs. 2e–h) are obtained by averaging these variables between 0° and 60°N, and 75° and 7.5°W, the domain commonly used to calculate the Atlantic multidecadal oscillation (AMO) index. While the multimodel-mean North Atlantic SST anomaly time series (Fig. 2g, black line) has much smaller amplitude than the observed counterpart (Fig. 2g, red line), the temporal correspondence between them is statistically significant: the cross-correlation coefficient between the simulated multimodel ensemble–mean AMO and observed AMO indices is 0.63 at zero lag; the most obvious mismatch occurred in the early part of the twentieth century, from 1900 to 1940.

The multimodel ensemble–mean detrended surface shortwave radiation flux anomaly (positive means downward; Fig. 2f) is negatively correlated with the detrended multimodel-mean AMOC index anomaly (Fig. 2b; also see Fig. 5, dashed line), and the maximum correlation occurs when the radiation flux anomaly leads the AMOC anomaly by roughly 10 yr. Taken together, when more shortwave radiation heats the ocean surface, AMOC slows down after 10 yr; at the same time, SST in the

North Atlantic warms up, as indicated by the positive correlation between shortwave radiation and SST anomalies at zero lag (Fig. 5, solid line). Because SST responds quicker to shortwave radiation forcing than the AMOC, it appears that SST anomaly leads the AMOC anomaly by 8–10 yr, and they are anticorrelated (Fig. 5, dotted line), meaning that warmer North Atlantic SST leads weaker AMOC by 8–10 yr.
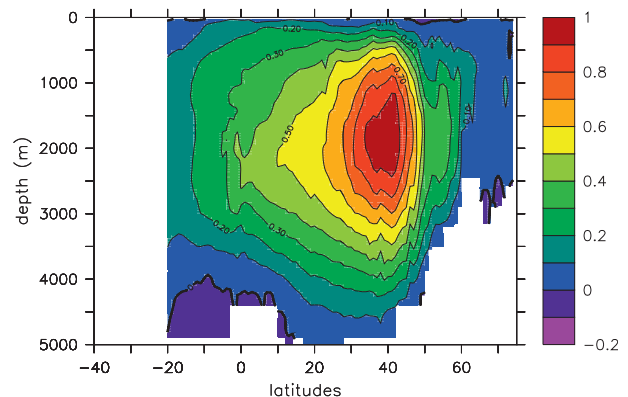

FIG. 4. Differences in the meridional overturning streamfunction obtained by subtracting the weakest third of the annual-mean streamfunctions from the strongest third of each model, then averaging across all models.
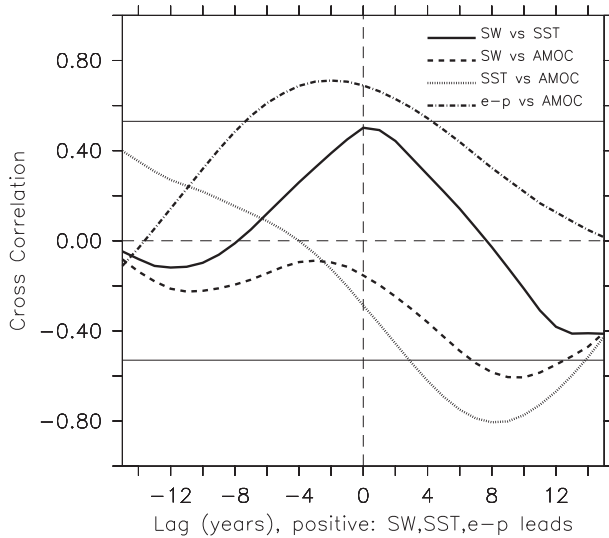
FIG. 5. Cross correlations between North Atlantic (0°–60°N, 75°–7.5°W) net surface shortwave radiative flux (positive indicates downward), subpolar region (40°–60°N, 75°–7.5°W) surface freshwater flux (positive indicates out of the ocean), SST, and the AMOC index anomalies shown in the right panels of Fig. 2. The thin horizontal lines mark the statistically significant value with a 95% confidence level.

c. North Atlantic SST and SSS anomaly spatial patterns

To explore the physical mechanisms linking surface shortwave forcing and the AMOC variability, we computed regression patterns of the shortwave radiation flux time series (Fig. 2f) on the North Atlantic SST (Fig. 6a) and sea surface salinity (SSS; Fig. 6b) fields at zero lags. Corresponding to increased basin mean downward shortwave radiation flux, the entire surface North Atlantic warms up (Fig. 6a); meanwhile, the subpolar (north of 40°N) and tropical (0°–40°N) North Atlantic becomes fresher while the subtropics (20°–40°N) are saltier (Fig. 6b). The SST response to shortwave forcing is thermally direct (more downward shortwave radiation leads to SST warming and vice versa). On the other hand, the SSS response (Fig. 6b) is consistent with results from a previous study (Delworth and Dixon 2006), which suggests that an increase in surface shortwave heating can strengthen the poleward atmospheric moisture transport, leading to more precipitation in the high latitudes and hence local SSS decrease and vice versa.

The SST and SSS anomalies associated with surface shortwave radiation fluctuation contribute to the same sign changes in surface density in the North Atlantic (Figs. 6a,b). To examine the relative contributions of salinity versus temperature effects, we used the linearized equation of state for seawater at the ocean surface: $\Delta\rho = -\alpha\Delta T + \beta\Delta S$, where α and β are thermal expansion and haline contraction coefficients, respectively. Assuming the mean SST in the North Atlantic is $\sim10°C$ and the mean SSS is ~35 psu, then $\alpha \approx 0.15\,\mathrm{kg\,m^{-3}\,°C^{-1}}$ and $\beta \approx 0.78\,\mathrm{kg\,m^{-3}\,psu^{-1}}$. Taking these values, the mean SST and SSS anomalies (ΔT and ΔS corresponding to $1\,\mathrm{W\,m^{-2}}$ change in the North Atlantic surface shortwave radiative flux) north of 40°N (Fig. 6, top) contribute to 0.018 and $0.023\,\mathrm{kg\,m^{-3}}$ sea surface density anomaly $\Delta\rho$, respectively. The salinity and temperature effects are on the same order of magnitude, with a slight dominance of saline over the thermal contribution.

Once the AMOC changes, it in turn can perturb the North Atlantic SST and SSS fields (Figs. 6c,d). Corresponding to a stronger AMOC, positive SSS anomalies develop in the subpolar North Atlantic (Fig. 6d), while the subtropical North Atlantic experiences a freshening anomaly. The SST anomalies in the subpolar latitudes in response to the AMOC changes (Fig. 6c) weaken the SST response to surface shortwave flux forcing (the opposite of Fig. 6a; notice Fig. 6a corresponds to increased downward shortwave flux and weakened AMOC states); in contrast, the feedbacks of the AMOC on SSS (Fig. 6d) reinforce the SSS anomalies in response to surface shortwave flux anomalies (the opposite of Fig. 6b; again, Fig. 6b corresponds to increased downward shortwave flux and weakened AMOC states).

4. Potential drivers of the twentieth-century multidecadal AMOC variability

We discussed the roles of two potential drivers; namely, the external climate forcing variability and the North Atlantic Oscillation (NAO) effect on the AMOC multidecadal variability in the twentieth century.

The phase of the multimodel ensemble–mean AMOC and North Atlantic surface shortwave flux variations (Figs. 2b,f) is very similar to aerosol forcing variability since 1860 [see Booth et al. (2012), their Fig. 4, for an observed aerosol time series]. Booth et al. (2012) exploited an approximately linear relationship between net surface shortwave radiation flux and total aerosol optical depth (e.g., Booth et al. 2012) to infer the effect of aerosols on the surface shortwave forcing. Similarly, we can interpret the surface shortwave flux variation in the North Atlantic basin, used in our analysis in section 3b, as representing decadal variability in external climate forcing, which is primarily influenced by surface aerosol (natural and anthropogenic) fluctuations. Impacts of aerosol forcing on the ocean circulation have been studied in single models before (e.g., Cai et al. 2006; Delworth and Dixon 2006). Delworth and Dixon (2006) argue that aerosol forcing can drive changes in the AMOC by perturbing surface buoyancy fluxes. The
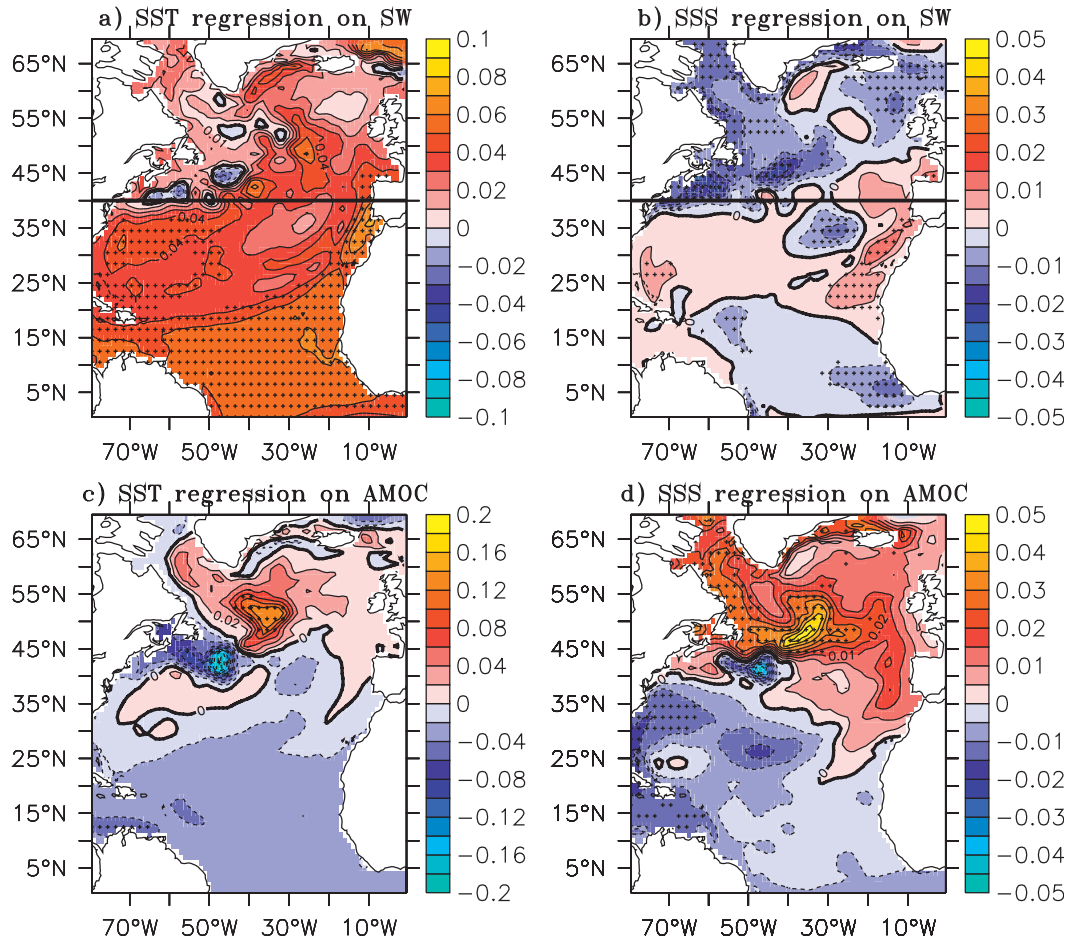
FIG. 6. Simultaneous regression maps of the North Atlantic (a) SST and (b) SSS anomalies on the net surface shortwave radiation flux anomaly time series shown in Fig. 2f. Simultaneous regression maps of North Atlantic (c) SST and (d) SSS on the AMOC index anomalies shown in Fig. 2b. Crosses indicate areas above the 95% confidence level.

regression maps presented in Figs. 6a and 6b are consistent with this argument. However, we bear in mind that surface shortwave radiation is also influenced by cloud feedbacks within the climate system; in addition, there are large uncertainties associated with direct and indirect aerosol effects and how they are represented in each model. Nonetheless, the results presented in section 3 suggest the existence of a common AMOC response to external climate forcing in multiple CMIP5 models.

The leading atmospheric variability mode in the North Atlantic is the NAO. NAO can drive multiple changes in the ocean including changes in the subpolar gyre circulation, surface buoyancy fluxes, and deep water formation in the northwestern Atlantic and therefore can have an impact on the AMOC. The station-based NAO index [following the definition by Hurrell and Deser (2009)] shows a spread among the models in CMIP5 (Fig. 7a)

that is expected from the known internal variability of the NAO. Averaging across all the models, the mean NAO index shows a weak upward trend over historical time (Fig. 7a); superimposed on this linear trend, the multimodel ensemble–mean NAO index shows a multidecadal variation that, generally speaking, increases from 1950 to 1980 and decreases from 1980 to the end of the century (Fig. 7b). Furthermore, there is close correspondence between the multimodel ensemble–mean NAO and the AMOC indices but only during the years 1950–2000, and this correspondence degraded in the earlier part of the twentieth century (Fig. 7b).

We again computed the combined EOFs of the multiple models' NAO indices. The first and second modes explain 37.3% and 21.1% of the total variance, respectively. The dominant low-frequency character of PC1 is an upward swing of the NAO from 1950 to 1980 and a decrease thereafter (Fig. 8a, solid line). The PC1 time
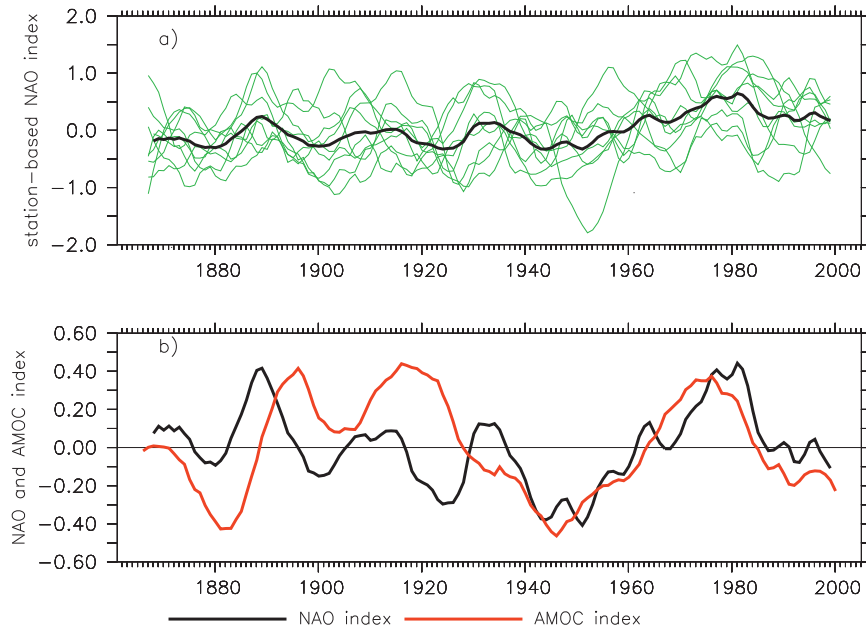
FIG. 7. (a) Difference in normalized December–March-mean sea level pressure between Lisbon, Spain, and Stykkisholmur, Iceland. Green lines are from each model's ensemble mean and the black line is the multimodel average. (b) Black line is the multimodel-mean NAO index from (a) but with the linear trend from 1850 to 2005 removed; red line is the detrended multimodel-mean AMOC index as shown in Fig. 2b.

series closely resembles the temporal variability of the multimodel-mean NAO index (Fig. 8a, dashed line), and a majority of the models project positively onto this mode (Fig. 8b). PC2 represents a multidecadal variation (Fig. 8c, solid line), and the corresponding eigenvalue amplitudes (Fig. 8d) show more noticeable variations across the models than the mode 1 eigenvalues do (Fig. 8b), although most of them still have the same sign.

Taken together, the multimodel ensemble–mean external climate forcing (as represented by the surface shortwave radiation flux into the North Atlantic basin), the NAO, and the AMOC appear to have coordinated changes in the second half of the twentieth century. Before the mid-twentieth century, the multimodel-mean multidecadal changes in the AMOC and climate forcing are consistent with one another, but the mean NAO index does not align with either of them.

5. Summary and discussion

We investigate whether the AMOC simulated by models in CMIP5 exhibits significant differences from CMIP3 simulations. In terms of the twentieth-century AMOC, results from 10 models in CMIP5 indicate a better correspondence toward observations than CMIP3 results. With regard to the AMOC trend in the twenty-first century under anthropogenic forcing scenarios, CMIP5

and CMIP3 give qualitatively similar predictions: the "best estimates" based on the CMIP3 A1B scenario suggests a 25%–30% weakening of the AMOC of the present day by year 2100 (Schneider et al. 2007); arithmetic averaging of the CMIP5 output gives a 21% (36%) weakening over the same time period under RCP4.5 (RCP8.5) scenarios. Notice that A1B forcing strength is between the RCP4.5 and RCP8.5 scenarios (Nakicenovic 2000).

Based on the multimodel-ensemble mean, we found a multidecadal variability of AMOC with an approximately 60-yr periodicity during years 1850–2005, the peak-to-peak amplitude is about 1 Sv; although small, it is not negligible relative to AMOC internal variability. All models project onto this multidecadal mode consistently, even though amplitudes are varied. Furthermore, this multidecadal AMOC variability is found to be significantly correlated with surface shortwave radiation flux anomalies in the North Atlantic with a phase lag: when downward shortwave radiation increases (decreases), AMOC slows down (speeds up) after about 10 yr. The multimodel-mean AMOC is also significantly correlated with surface freshwater flux anomalies averaged in the subpolar North Atlantic, and the maximum correlation occurs when the AMOC leads the freshwater flux anomaly by roughly 2 yr. Because decadal fluctuations in the net surface shortwave flux anomalies are closely related to
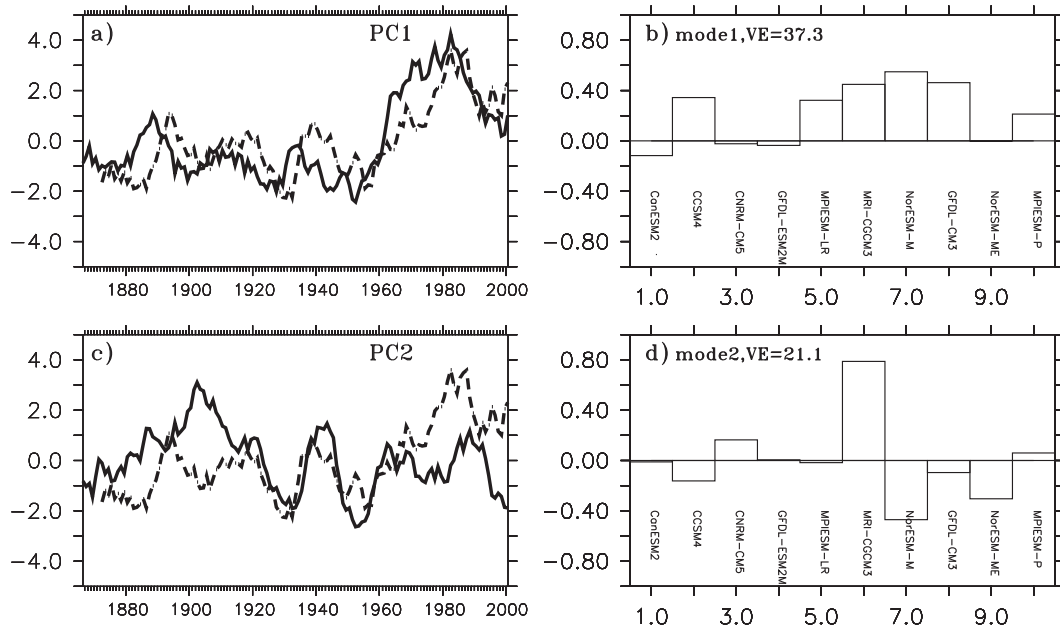
FIG. 8. Eigenvalue decomposition of multimodel NAO indices. Similarly to the multimodel AMOC index decomposition (results shown in Fig. 3), we combined each model's NAO indices into one matrix and computed the EOFs of this matrix. First two modes are shown. (b),(d) The x axis corresponds to the 10 models used in this study. Variance explained by each mode is marked in the right panels. (a),(c) The dashed line is the multimodel ensemble–mean NAO anomaly time series from Fig. 7a (scaled by a factor of 6 for displaying purposes).

external forcing variability, such as those associated with either anthropogenic or volcanic surface aerosols, these results suggest a common AMOC response to external climate forcing variations across multiple models in CMIP5. Moreover, the ensuing positive feedbacks of the AMOC changes on the North Atlantic freshwater flux (stronger AMOC → warm subpolar latitude SST anomalies → stronger evaporation and therefore more surface buoyancy loss → even stronger AMOC and vice versa) further reinforce the AMOC response. Mechanistically, the North Atlantic surface shortwave flux anomaly can perturb the AMOC through perturbing surface buoyancy fluxes in the subpolar latitudes (Delworth and Dixon 2006). The common AMOC response in the second half of the twentieth century is concurrent with the multimodel ensemble–mean NAO index: they both show an upward trend between years 1950 and 2000; on top of this linear trend, there is a multidecadal fluctuation that peaks around year 1980, and 7 out of the 10 models in CMIP5 examined in this study demonstrate this temporal character.

The multimodel ensemble–mean SST anomalies in the North Atlantic bear temporal resemblance to the observed AMO index (Fig. 2g), but the amplitude is substantially smaller. We note that the same AMO-like multidecadal variation was found by Chiang et al. (2013) in the multimodel-mean CMIP5 historical simulations as

expressed in the Atlantic interhemispheric SST gradient (and also with significantly muted amplitude). The mechanisms behind AMO are still debated (Delworth and Mann 2000; Ting et al. 2009; Deser et al. 2010; Booth et al. 2012). Using CMIP3 output and vigorous statistics, Ting et al. (2009) attributed the multidecadal ''oscillation'' in the observed twentieth-century AMO index primarily to internal variability; Booth et al. (2012), however, implicated aerosol forcing as the main driver for the twentieth-century North Atlantic SST variability in the Hadley Centre Earth System Model. The interrelationships between the multimodel-mean AMOC, North Atlantic SST, and surface shortwave radiation flux anomalies explored in this study suggest that the phasing of North Atlantic SST variability from the late-nineteenth-century to twentieth-century is generally consistent with external climate forcing variations (as represented by the North Atlantic basin–averaged shortwave radiation flux anomalies), but the amplitude would be much weaker if driven by external forcing alone.

The main caveats of this study are the finite number of ensemble runs and intermodel variations in forcing as well as model physics. The multimodel ensemble–mean approach assumes a common external forcing applied across all models, which was the design behind Coupled Model Intercomparison Project framework; however, how the external forcing is felt in each model can still

vary substantially. Regardless, the combined EOF analysis in section 2 supports the existence of a common model response by the AMOC to the applied external forcing. Ultimately, the examination of single-forcing runs of individual models is required in order to properly attribute the influence of specific forcing agents on the AMOC.

APPENDIX

Use of Model Data

TABLE A1. CMIP5 models used in this study, their expansions, and their numbers of ensemble runs in historical (1850–2005) and RCP simulations. The dash indicates no run is available under that forcing scenario and time period.

Model names	Historical runs (1850–2005)	RCP4.5 runs		RCP8.5 runs	
		2006–2100	2101–2300	2006–2100	2101–2300
Second Generation Canadian Earth System Model (CanESM2)	5	5	2	5	—
Community Climate System Model, version 4 (CCSM4)	6	5	1	4	—
Centre National de Recherches Météorologiques Coupled Global Climate Model, version 5 (CNRM-CM5)	10	1	—	1	—
Geophysical Fluid Dynamics Laboratory Earth System Model with Modular Ocean Model 4 (MOM4) component (GFDL-ESM2M)	1	1	—	1	—
Max Planck Institute Earth System Model, low resolution (MPI-ESM-LR)	3	3	1	3	1
Meteorological Research Institute Coupled Atmosphere–Ocean General Circulation Model, version 3 (MRI-CGCM3)	5	1	—	1	—
Norwegian Earth System Model, version 1 (intermediate resolution) (NorESM1-M)	3	1	1	1	—
Geophysical Fluid Dynamics Laboratory Climate Model, version 3 (GFDL CM3)	5	1	—	1	—
Norwegian Earth System Model, version 1 (intermediate resolution with carbon cycle) (NorESM1-ME)	1	1	—	—	—
Max Planck Institute Earth System Model, paleo (MPI-ESM-P)	2	—	—	—	—

REFERENCES

Booth, B. B. B., N. J. Dunstone, P. R. Halloran, T. Andrews, and N. Bellouin, 2012: Aerosols implicated as a prime driver of twentieth-century North Atlantic climate variability. *Nature,* **484,** 228–232, doi:10.1038/nature10946.

Bryden, H. L., A. Mujahid, S. A. Cunningham, and T. Kanzow, 2009: Adjustment of the basin-scale circulation at 26°N to variations in Gulf Stream, deep western boundary current and Ekman transports as observed by the RAPID array. *Ocean Sci.,* **5,** 421–433.

Cai, W., D. Bi, J. Church, T. Cowan, M. Dix, and L. Rotstayn, 2006: Pan-oceanic response to increasing anthropogenic aerosols: Impacts on the Southern Hemisphere oceanic circulation. *Geophys. Res. Lett.,* **33,** L21707, doi:10.1029/2006GL027513.

Cheng, W., R. Bleck, and C. Rooth, 2004: Multi-decadal thermohaline variability in an ocean–atmosphere general circulation model. *Climate Dyn.,* **22,** 573–590.

——, C. M. Bitz, and J. C. H. Chiang, 2007: Adjustment of the global climate to an abrupt slowdown of the Atlantic meridional overturning circulation. *Ocean Circulation: Mechanisms and Impacts—Past and Future Changes of Meridional Overturning, Geophys. Monogr.,* Vol. 173, Amer. Geophys. Union, 295–313.

Chiang, J. C. H., W. Cheng, and C. M. Bitz, 2008: Fast teleconnections to the tropical Atlantic sector from Atlantic thermohaline adjustment. *Geophys. Res. Lett.,* **35,** L07704, doi:10.1029/2008GL033292.

——, C.-Y. Chang, and M. F. Wehner, 2013: Long-term behavior of the Atlantic interhemispheric SST gradient in the CMIP5 historical simulations. *J. Climate,* in press.

Cunningham, S. A., and Coauthors, 2007: Temporal variability of the Atlantic meridional overturning circulation at 26.5°N. *Science,* **317,** 935–938.

Danabasoglu, G., S. G. Yeager, Y.-O. Kwon, J. J. Tribbia, A. S. Phillips, and J. W. Hurrell, 2012: Variability of the Atlantic meridional overturning circulation in CCSM4. *J. Climate,* **25,** 5153–5172.

Delworth, T. L., and M. E. Mann, 2000: Observed and simulated multidecadal variability in the Northern Hemisphere. *Climate Dyn.,* **16,** 661–676.

——, and K. W. Dixon, 2006: Have anthropogenic aerosols delayed a greenhouse gas-induced weakening of the North Atlantic thermohaline circulation? *Geophys. Res. Lett.,* **33,** L02606, doi:10.1029/2005GL024980.

——, S. Manabe, and R. J. Stouffer, 1993: Interdecadal variations of the thermohaline circulation in a coupled ocean–atmosphere model. *J. Climate,* **6,** 1993–2011.

——, and Coauthors, 2012: Simulated climate and climate change in the GFDL CM2.5 high-resolution coupled climate model. *J. Climate,* **25,** 2755–2781.

Deser, C., M. A. Alexander, S.-P. Xie, and A. S. Phillips, 2010: Sea surface temperature variability: Patterns and mechanisms. *Annu. Rev. Mar. Sci.,* **2,** 115–143.

Ganachaud, A., 2003: Large-scale mass transports, water mass formation, and diffusivities estimated from World Ocean Circulation Experiment (WOCE) hydrographic data. *J. Geophys. Res.,* **108,** 3213, doi:10.1029/2002JC001565.

Gregory, J. M., and Coauthors, 2005: A model intercomparison of changes in the Atlantic thermohaline circulation in response to increasing atmospheric CO_2 concentration. *Geophys. Res. Lett.,* **32,** L12703, doi:10.1029/2005GL023209.

Hu, A., G. A. Meehl, W. Han, and J. Yin, 2011: Effect of the potential melting of the Greenland ice sheet on the meridional overturning circulation and global climate in the future. *Deep-Sea Res. II,* **58,** 1914–1926.

Hurrell, J. W., and C. Deser, 2009: North Atlantic climate variability: The role of the North Atlantic Oscillation. *J. Mar. Syst.,* **78,** 28–41.

Johns, W. E., and Coauthors, 2011: Continuous, array-based estimates of Atlantic Ocean heat transport at 26.5°N. *J. Climate,* **24,** 2429–2449.

Joyce, T. M., and R. Zhang, 2010: On the path of the Gulf Stream and the Atlantic meridional overturning circulation. *J. Climate,* **23,** 3146–3154.

Kanzow, T., and Coauthors, 2010: Seasonal variability of the Atlantic meridional overturning circulation at 26.5°N. *J. Climate,* **23,** 5678–5698.

Kwon, Y.-O., and C. Frankignoul, 2012: Stochastically-driven multidecadal variability of the Atlantic meridional overturning circulation in CCSM3. *Climate Dyn.,* **38,** 859–876.

Levermann, A., A. Griesel, M. Hofmann, M. Montoya, and S. Rahmstorf, 2005: Dynamic sea level changes following changes in the thermohaline circulation. *Climate Dyn.,* **24,** 347–354.

Lumpkin, R., and K. Speer, 2007: Global ocean meridional overturning. *J. Phys. Oceanogr.,* **37,** 2550–2562.

Meehl, G. A., and Coauthors, 2007: Global climate projections. *Climate Change 2007: The Physical Science Basis,* S. Solomon et al., Eds., Cambridge University Press, 747–845.

Nakicenovic, N., 2000: Greenhouse gas emissions scenarios. *Technol. Forecasting Soc. Change,* **65,** 149–166.

Rayner, D., and Coauthors, 2011: Monitoring the Atlantic meridional overturning circulation. *Deep-Sea Res. II,* **58,** 1744–1753.

Sabine, C. L., and Coauthors, 2004: The oceanic sink for anthropogenic CO_2. *Science,* **305,** 367–371.

Schmittner, A., M. Latif, and B. Schneider, 2005: Model projections of the North Atlantic thermohaline circulation for the 21st century assessed by observations. *Geophys. Res. Lett.,* **32,** L23710, doi:10.1029/2005GL024368.

Schneider, B., M. Latif, and A. Schmittner, 2007: Evaluation of different methods to assess model projections of the future evolution of the Atlantic meridional overturning circulation. *J. Climate,* **20,** 2121–2132.

Smethie W. M., Jr., and R. A. Fine, 2001: Rates of North Atlantic Deep Water formation calculated from chlorofluorocarbon inventories. *Deep-Sea Res. I,* **48,** 189–215.

Solomon, S., D. Qin, M. Manning, Z. Chen, M. Marquis, K. Averyt, M. B. Tignor, and H. L. Miller Jr., Eds., 2007: *Climate Change 2007: The Physical Science Basis.* Cambridge University Press, 996 pp.

Sutton, R. T., and D. L. R. Hodson, 2005: Atlantic Ocean forcing of North American and European summer climate. *Science,* **309,** 115–118.

Talley, L. D., J. L. Reid, and P. E. Robbins, 2003: Data-based meridional overturning streamfunctions for the global ocean. *J. Climate,* **16,** 3213–3226.

Taylor, K. E., R. J. Stouffer, and G. A. Meehl, 2012: An overview of CMIP5 and the experiment design. *Bull. Amer. Meteor. Soc.,* **93,** 485–498.

Ting, M., Y. Kushnir, R. Seager, and C. Li, 2009: Forced and internal twentieth-century SST trends in the North Atlantic. *J. Climate,* **22,** 1469–1481.

Vellinga, M., and R. A. Wood, 2002: Global climatic impacts of a collapse of the Atlantic thermohaline circulation. *Climatic Change,* **54,** 251–267.

Wang, C., S. Dong, and E. Munoz, 2010: Seawater density variations in the North Atlantic and the Atlantic meridional overturning circulation. *Climate Dyn.,* **34,** 953–968.

Woollings, T., J. M. Gregory, J. G. Pinto, M. Reyers, and D. J. Brayshaw, 2012: Response of the North Atlantic storm track to climate change shaped by ocean-atmosphere coupling. *Nat. Geosci.,* **5,** 313–317.

Zhang, R., and T. L. Delworth, 2006: Impact of Atlantic multidecadal oscillations on India/Sahel rainfall and Atlantic hurricanes. *Geophys. Res. Lett.,* **33,** L17712, doi:10.1029/2006GL026267.